Acta Pharmaceutica Sinica B 2023;13(12):4999–5015

Chinese Pharmaceutical Association
Institute of Materia Medica, Chinese Academy of Medical Sciences

Acta Pharmaceutica Sinica B

www.elsevier.com/locate/apsb
www.sciencedirect.com

ORIGINAL ARTICLE

Hippo pathway-manipulating neutrophil-mimic hybrid nanoparticles for cardiac ischemic injury *via* modulation of local immunity and cardiac regeneration

Qiaozi Wang[a,d,†], Yanan Song[a,d,†], Jinfeng Gao[a,d,†], Qiyu Li[a,d], Jing Chen[a,d], Yifang Xie[b], Zhengmin Wang[a,d], Haipeng Tan[a,d], Hongbo Yang[a,d], Ning Zhang[a,d], Juying Qian[a,d], Zhiqing Pang[c,*], Zheyong Huang[a,d,*], Junbo Ge[a,b,d,*]

[a]*Department of Cardiology, Zhongshan Hospital, Fudan University, Shanghai Institute of Cardiovascular Diseases, Shanghai 200032, China*
[b]*Institute of Biomedical Sciences, Fudan University, Shanghai 200032, China*
[c]*School of Pharmacy, Fudan University, Key Laboratory of Smart Drug Delivery, Ministry of Education, Shanghai 201203, China*
[d]*National Clinical Research Center for Interventional Medicine, Shanghai 200032, China*

Received 3 May 2023; received in revised form 19 July 2023; accepted 28 July 2023

KEY WORDS

Myocardial infarction;
Cardiac regeneration;
Biomimetic nanoparticles;
Neutrophils;
Immunity restoration;
MicroRNA;
Hippo pathway;
Membrane fusion

Abstract The promise of regeneration therapy for restoration of damaged myocardium after cardiac ischemic injury relies on targeted delivery of proliferative molecules into cardiomyocytes whose healing benefits are still limited owing to severe immune microenvironment due to local high concentration of proinflammatory cytokines. Optimal therapeutic strategies are therefore in urgent need to both modulate local immunity and deliver proliferative molecules. Here, we addressed this unmet need by developing neutrophil-mimic nanoparticles NM@miR, fabricated by coating hybrid neutrophil membranes with artificial lipids onto mesoporous silica nanoparticles (MSNs) loaded with microRNA-10b. The hybrid membrane could endow nanoparticles with strong capacity to migrate into inflammatory sites and neutralize proinflammatory cytokines and increase the delivery efficiency of microRNA-10b into adult mammalian cardiomyocytes (CMs) by fusing with cell membranes and leading to the release of MSNs-miR into

*Corresponding authors.
E-mail addresses: zqpang@fudan.edu.cn (Zhiqing Pang), zheyonghuang@126.com (Zheyong Huang), junboge@126.com (Junbo Ge).
[†]These authors made equal contributions to this work.
Peer review under the responsibility of Chinese Pharmaceutical Association and Institute of Materia Medica, Chinese Academy of Medical Sciences.

https://doi.org/10.1016/j.apsb.2023.08.021

cytosol. Upon NM@miR administration, this nanoparticle could home to the injured myocardium, restore the local immunity, and efficiently deliver microRNA-10b to cardiomyocytes, which could reduce the activation of Hippo-YAP pathway mediated by excessive cytokines and exert the best proliferative effect of miR-10b. This combination therapy could finally improve cardiac function and mitigate ventricular remodeling. Consequently, this work offers a combination strategy of immunity modulation and proliferative molecule delivery to boost cardiac regeneration after injury.

1. Introduction

Adult mammalian cardiomyocytes (CMs) almost lose their capacity for proliferation so that they could not regenerate in response to the external injury, which is the major reason for the heavy burden of the cardiovascular diseases nowadays[1]. Recently, a promising strategy to improve the outcome is to restore the impaired myocardium by promoting endogenous CMs proliferation[2]. The Hippo-YAP pathway, a highly conserved intracellular axis, plays a crucial role in fetal heart growth and the progression of cardiac diseases by regulating the proliferation and death of CMs[3]. Several studies have demonstrated that activation of YAP induces CM proliferation in mice[4,5] suggesting the potential possibility to manipulate Hippo-YAP pathway to improve the treatment of cardiac ischemic injury. Notably, several microRNAs (miRNAs), have been reported to play important roles in the regulation of the Hippo-YAP pathway in the heart[6–9]. We previously reported that miRNA-10b-5p (miR-10b) could promote proliferation of human embryonic stem cell-derived cardiomyocytes (hESC-CMs) by targeting *LATS1* in the Hippo pathway and increasing nuclear entry of YAP, suggesting its potential role in cardiac regeneration therapy by regulating Hippo-YAP pathway[8].

Despite these promising benefits, several drawbacks have restrained further progress of miRNA therapy to regulate Hippo signaling pathway in clinical translation. A rapid inflammatory response is triggered and massive proinflammatory cytokines are released in injured myocardium after cardiac ischemic injury. These redundant proinflammatory cytokines may lead to the degradation of YAP protein and activate Hippo-YAP pathway, which may impair endogenous CM proliferation under cardiac injury[3,5,10,11]. Simply delivering miRNAs to regulate Hippo-YAP pathway may not bring about expected therapeutic results in myocardial ischemia injury. Neutralization of local proinflammatory cytokines may be beneficial to improving the outcome of cardiac injury. Both basic research and clinical studies have witnessed the preliminary improvement of myocardial infarction by utilizing U.S. Food and Drug Administration (FDA)-approved anti-IL-1β monoclonal antibody (Canakinumab) as anti-inflammatory therapy[12,13]. However, since several proinflammatory cytokines play important roles after acute cardiac injury, neutralizing or removing a single specific cytokine may have a limited effect due to some latent compensation mechanisms. Recently, cell membrane-coated nanoparticles have emerged as a promising therapeutic platform for the sponging of multiple cytokines, such as neutrophil and macrophage membrane-based therapy[14–17]. Nonetheless, such nanodecoys in these research are composed of pure cell membranes with negative charge, which is not the best approach for increasing interaction between nanoparticles and the recipient cells. Moreover, miRNAs are unstable due to degradation by ribonucleases *in vivo*. Therefore, it's of great need to develop novel strategies that could both absorb local proinflammatory cytokines to regulate microenvironment and deliver therapeutic miRNAs efficiently to target cells.

To address those issues, we aimed to employ the neutrophil-like nanoparticle (NM@miR) which simultaneously restores the immune microenvironment and delivers miR-10b to regulate the Hippo-YAP pathway and promote the proliferation of pre-existing CMs. Specifically, we developed NM@miR by coating hybrid biomimetic nanovesicles composed of neutrophil membranes and artificial cationic lipids DOTAP onto mesoporous silica nanoparticles (MSNs) loaded with the therapeutic miR-10b to regulate Hippo pathway (Fig. 1). The addition of cationic lipids DOTAP, which has been proved to mediate the membrane fusion process between nanomaterials and the target cells[18–21], endows the neutrophil-like membrane the ability to fuse with the target cell membranes and let the release of inner parts. MSNs, with a large capacity of carrying nucleic acids, are suitable for delivering miRNAs[22–24]. Combination of the hybrid biomimetic membrane and MSNs core helped protect microRNA from degradation and presented a well-behaved long circulation profile due to the neutrophil membrane camouflage. The as-prepared NM@miR inherited most membrane receptors from neutrophils with a right-side-out receptor orientation on the surface, enabling them to migrate into inflammatory site and act as traps to neutralize inflammatory cytokines. In a mouse model of myocardial ischemic reperfusion (I/R) injury, this neutrophil membrane vesicle (NMV)-camouflaged nanosponge could mimic recruited neutrophils to home to the infarcted myocardium after transmigrating across the endothelial cells and have a strong capacity to absorb cytokines *in vivo*, which otherwise would mediate degradation of YAP protein and activation of Hippo pathway to impair endogenous CM proliferation. Meanwhile, NM@miR could be uptake by CMs and membrane fusing of NM@miR and CMs allows release of therapeutic payload miR-10b, which could promote CMs proliferation by negatively regulating Hippo pathway (Fig. 1). This combination of immune microenvironment reconstruction and regeneration therapy could make the best use of therapeutic miR-10b and prevent severe cardiac modelling and eventual heart failure. We suppose that this combination therapy will provide new insights for regeneration therapy after cardiac ischemic injury. The potency of this biomimetic nanosponge to modulate immune microenvironment by absorbing proinflammatory cytokines and to promote the CMs proliferation was carefully investigated.

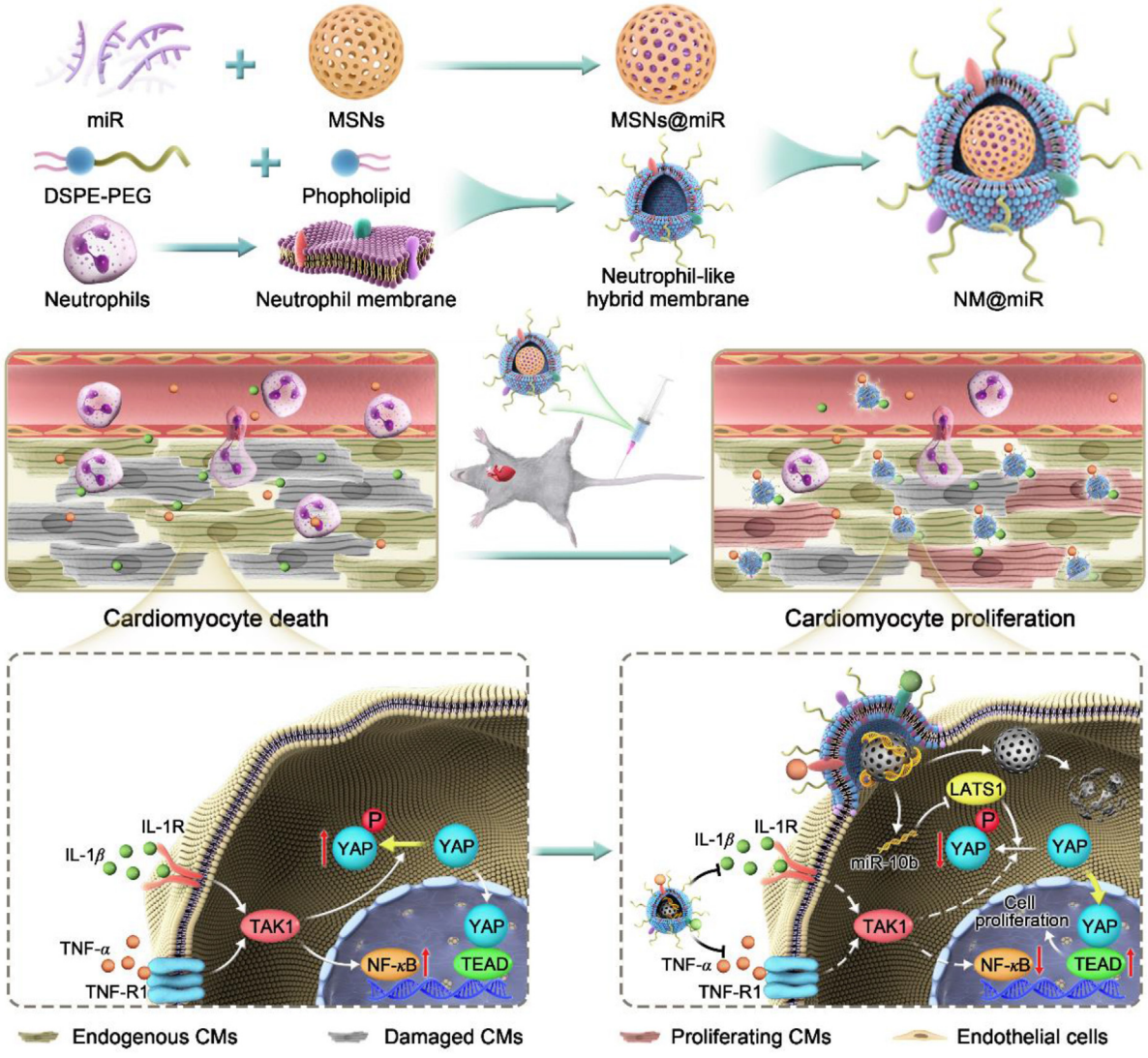

Figure 1 Schematic illustration of preparation process of NM@miR and how it performs effect of cytokine absorption and cardiomyocyte proliferation in a mouse model of myocardial ischemia/reperfusion injury.

2. Materials and methods

2.1. *Neonatal mouse ventricular CMs isolation and culture*

Neonatal mouse ventricular CMs were isolated by enzymatic digestion of postnatal 1.5 C57BL/6 mice. Briefly, neonatal mice were killed *via* 2% isoflurane inhalation. Hearts were dissected and cut into 1 mm^3 pieces using the razor. Then the tissues were digested in collagenase buffer [0.08% Collagenase Type I (Worthington, NJ, USA) diluted in Hank's balanced salt solution (Solarbio, Beijing, China)] 5 min at 37 °C for 5−6 times. Each time the cell suspension supernatant was collected and neutralized in equal volume of culture media and filtered through 70 μm cell strainer (BD Falcon, Corning, NY, USA). Then the supernatant was centrifuged, and the pellet was resuspended Dulbecco's modified Eagle's medium (DMEM) with 10% fetal bovine serum and 100 × penicillin/streptomycin (P/S), followed by seeding into 10 cm dishes for 1 h 30 min at 37 °C. After that, the supernatant containing neoCMs was then pelleted, resuspended in fresh DMEM plus 10% FBS and P/S in the gelatin-coated dishes.

2.2. *Transfection*

Mir-10b mimics and their negative controls (GenePharma, Shanghai, China) were transfected into CMs using Lipofectamine RNAiMAX (Invitrogen, Carlsbad, CA, USA) according to the instructions at a final concentration of 50 μmol/L. Six hours after transfection, CMs were changed with fresh medium.

2.3. *Luciferase reporter assay*

The psiCHECK plasmid was constructed by inserting the binding area fragment of miR-10b and the 3′ UTR of *Lats1*, into the backbone plasmid by Gibson Assembly. The fragment was amplified from the mouse genome. The mutant plasmid was also constructed using specific primers. 293T cells were passaged into 24-well plates. Twelve hours later, the cells were co-transfected

with the plasmids and mimics or related controls by using Lipofectamine 2000 (Invitrogen, Carlsbad, CA, USA). 48 h after transfection, the luciferase levels were measured and calculated according to manufacturer's protocol using the Dual-Luciferase Assay Kit (Promega, Madison, WI,USA).

2.4. Western blot analysis

CMs were first washed with phosphate buffer saline (PBS) before scratched off from the plates and lysed with RIPA buffer with complete protease inhibitor cocktail (Takara, Japan). After boiling together with 6 × SDS loading buffer, samples were loaded onto 4%−15% Mini-PROTEN Precast protein gels (BioRad, Hercules, CA, USA). The separated proteins were transferred onto nitrocellulose membranes (BioRad, Hercules, CA, USA) for about 1.5 h. Next, blocking buffer, Tris buffered saline with Tween (TBST) with 5% bovine serum albumin (BSA), was added to block non-specific interaction of the membranes for 1 h at room temperature, followed by overnight incubating with different primary antibodies at 4 °C. The next day, after washing with TBST by 3 times, 10 min for each time, the membranes were incubated with related secondary antibodies for 1 h at room temperature. After another three times TBST washing, membranes were emerged with SuperSignal chemiluminescence solutions (ThermoFisher, Carlsbad, CA, USA) and images were obtained with BioRad Imaging System.

2.5. Immunofluorescence

CMs were first washed with PBS for 3 min three times and then fixed with 4% paraformaldehyde (PFA) for 15 min followed by another three times PBS washing. Cells were then permeabilized by 0.1% Triton X-100 in PBS for 15 min. Next, cells were blocked with 3% BSA in PBS for 1 h at room temperature and then incubated with the following primary antibodies at 4 °C: Ki67 (CST, Danvers, MA, USA), cTnT (Proteintech, Rosemont, IL, USA), and PH3 (Abcam, Waltham, MA, USA). After overnight incubation, CMs were incubated with fluorescence conjugated secondary antibodies (Alexa Fluor 488, 568, Abcam, Waltham, MA, USA) for 1 h at room temperature. Finally, to visualize nuclei, the cells were stained with DAPI (Sigma, Burbank, CA, USA) diluted in PBS. For EdU staining, 5 mmol/L 5-ethynyl-2' deoxy uridine was added to the culture medium 24 h before the start of immunofluorescence staining. The proliferative cells were imaging with the Click-IT EdU Imaging Kit (Invitrogen, Carlsbad, CA, USA) following the manufacturer's protocol, before DAPI staining.

2.6. RNA extraction and qRT-PCR

Total RNA was extracted by Trizol (Invitrogen, Carlsbad, CA, USA) following the manufacturer's protocol. RNA was then synthesized into complementary DNA (cDNA) with SuperScript™ IV VILO™ Master Mix (Invitrogen, Carlsbad, CA, USA). qRT-PCR was performed to quantitatively measure mRNA levels using SYBR Green Master Mix (Invitrogen, Carlsbad, CA, USA) on the Applied Biosystems qPCR machine, and β-Actin was chosen as the housekeeping gene in the following experiments. To measure the expression level of miRNA, the miScript Reverse Transcription Kit (QIAGEN, Hilden, Germany) and the miScript SYBR Green PCR Kit (QIAGEN, Hilden, Germany) were used. The U6 gene was chosen as a negative control.

2.7. Neutrophil collection, activation, and membrane derivation

Mouse neutrophils were collected from bone marrow of C57BL/6 mice using a mouse neutrophil isolation kit (Solarbio, Beijing, China) according to the manufacturer's instructions. Briefly, after removal of muscle, murine femurs and tibias were immersed in RPMI 1640 medium (Gibco, Carlsbad, CA, USA). Then the bone marrows were flushed form bone with the medium, centrifuged at 13,000 rpm (Eppendorf 5425, Hamburg, Germany) for 5 min at 4 °C and resuspended in buffer B. The suspension was added into buffer A and buffer C in sequence, followed by centrifugation at $800\times g$ for 20 min at 25 °C. The cell contents between the interface of buffer A and buffer C were collected. The collected neutrophils were then washed with ice-cold PBS and were then activated after incubation in RPMI medium with recombinant mouse TNF-α (50 ng/mL, Peprotech, NJ, USA) for 6 h at 37 °C. Activated neutrophils were washed with cold PBS and resuspended in hypotonic lysis buffer (30 mmol/L Tris-HCl, 225 mmol/L D-mannitol, 0.2 mmol/L ethylene glycol-bis(β-aminoethyl ether)-*N*,*N*,*N*′,*N*′-tetraacetic acid (EGTA) and 75 mmol/L sucrose with protease and phosphatase inhibitor cocktail). The suspensions were homogenized using a Dounce homogenizer for about 20 times, followed by centrifugation at $20{,}000\times g$ for 25 min at 4 °C. After that the cell debris was discarded and further centrifugated at $100{,}000\times g$ for 35 min. The pellet in the bottom of the centrifuge tube was resuspended with ethylene diamine tetraacetic acid (EDTA) buffer.

2.8. Nanoparticle preparation

MSNs were prepared following the previous reported method[25]. Briefly, 150 μL of triethanol amine and 3 g hexadecyl trimethyl ammonium bromide were both added into 60 mL distilled H_2O and the mixture was heated at 60 °C for 1 h. 4 mL of tetraethyl orthosilicate and 16 mL of cyclohexane were further added into the reaction mixture and stirred continuously for 24 h. Then the mixture was centrifuged at 13,000 rpm (Eppendorf 5810R, Hamburg, Germany) for 5 min to obtain the products which were redispersed using ethanol. To remove the remaining CTAB, ethanol was added to the dispersed MSNs and stirred for 3 h. The final products were dissolved in PBS. PEI-functionalized MSNs (PEI-MSNs) were synthesized by mixing with MSNs and poly (ethylene imine) (PEI) in distilled water for 2 h. After the synthesis of MSNs, they were redispersed and stirred with deionized water containing 0.3 g PEI for about 2 h. After that, the products were washed by absolute ethyl alcohol for several times. Extra PEI was removed by washing with absolute ethyl alcohol. 500 nmol/L miRNA mimics were mixed with PEI-MSNs for 6 h at 4 °C. MSNs@miR were obtained after centrifugation and resuspended in PBS in order to remove excessive miRNA mimics. For hybrid neutrophil membrane coating, lipids including DMPC, DOTAP, and DSPE-PEG_{2000}-NHS (Avanti Polar Lipids, Canada) at the molar ratio of 76.2:20:8 were weighed and dissolved in chloroform. Then the lipid layers were prepared by thin film hydration method as previously reported and rehydrated using PBS containing MSNs@miR followed by sonication for 10 min. To prepare hybrid membrane, the lipid solutions were mixed with aqueous solution of neutrophil membranes at different weight ratios and sequentially extruded using polycarbonate porous membranes of different size (1 μm, 400 and 200 nm). The final NM@miR was collected by centrifugation at 13,000 rpm for 5 min after removing of excess lipid, neutrophil membrane and resuspended in PBS for use.

2.9. Nanoparticle characterization

Transmission electron microscope (TEM) images were acquired by JEOL 1200 EX II TEM. The size and zeta potential of nanoparticles were measured by dynamic light scattering (DLS) using a Malvern Zetasizer Nano ZS. For verification of the colocalization of neutrophil membrane protein and lipid, we used fluorescence lipid DiD-DSPE-PEG (Xi'an Ruixi Biological, Xi'an, China) for synthesizing the nanoparticles, and NMV was labeled with commercial protein label kit from ThermoFisher Scientific (CA, Carlsbad, USA), which can react with exposed N-terminal α-amino groups of lysine residues to form stable amide bonds. After that, samples prepared by either simply pipetting or serial extrusion were imaged using Olympus FV3000. The colocalization analysis was performed by using the ImageJ-Fiji Software (National Institute of Health, USA). Texas Red-X-conjugated WGA (Invitrogen, Carlsbad, CA, USA) was utilized to investigate the orientation of membrane proteins on the nanoparticles. Briefly, Nanoparticles (MSNs@miR and NM@miR) were incubated with 10 μg/mL of fluorescent WGA in PBS for 30 min and unbound WGA was washed away by dialysis. NMVs were regarded as positive control. Then the fluorescence intensity was quantified under the microplate reader. To investigate the protection of hybrid lipid on miRNA degradation from surrounding environment, 5 μL RNase A (Beyotime, Shanghai, China) was added into the 100 μL of miRNA solution in the form of NM@miR or in the free form. After incubation at 37 °C for different time points (0, 0.5, 1 and 2 h), the samples were loaded into 1% agarose gel followed by running for 20 min at 120 V. The gel was further visualized by Bio-Rad Image Lab. To examine the uptake of nanoparticles by macrophages, murine RAW 264.7 macrophages were incubated with NM@miR and MSNs@miR (with DiD-labeled Lipid) for 24 h before washing with PBS. Then cells were fixed with 4% PFA, blocked with 3% BSA in PBS and stained with anti-F4/80 primary antibody (Abcam, Waltham, MA, USA) at 4 °C overnight. The next day, Alexa Fluor488 conjugated-secondary antibody was used after washing with PBS for 3 times. Cells were imaged under confocal microscope after another three times washed and staining with DAPI for 15 min.

2.10. Construction of myocardial ischemia/reperfusion injury model

All mice were housed in a specific pathogen-free experimental animal center at Zhongshan Hospital Fudan University. All experimental procedures were executed according to the protocols approved by The Animal Ethics Committee of Zhongshan Hospital Fudan University. 6−8 weeks old C57BL/6 mice were habituated to the animal facilities for 1 week before surgery. After anesthesia with 2% isoflurane, mice were intubated, ventilated with a RoVent Jr. Standard Ventilator. The heart was exposed by dissecting the intercostal muscle and then the left anterior descending (LAD) artery was temporally ligated for 40 min with a 7-0 silk suture. Then the chest was closed, mice were allowed to recover on the heating pad.

2.11. Quantification of cytokines concentration

Quantification of IL-1β, IL-6 and TNF-α was performed in different conditions. For cytokine binding with nanoparticles, recombinant cytokines were mixed with NM@miR, RM@miR, MSNs@miR, and NM@miR plus inhibitor of certain cytokine receptor at different concentrations. The mixtures were incubated for 2 h at 37 °C and then centrifugated at 20,000 rpm (Eppendorf 5424R, Hamburg, Germany) for 20 min at 4 °C. The supernatant was collected for further measurement. For binding capacity of nanoparticles with cytokines in the serum, 6−8 weeks old C57BL/6 mice were subjected to mouse myocardial I/R injury model and serum was isolated 6 h after the surgery, followed by mixing with NM@miR, RM@miR, MSNs@miR, and NM@miR plus inhibitor of certain cytokine receptor at different concentrations immediately. The mixtures were incubated for 2 h at 37 °C and then centrifugated at 20,000 rpm for 20 min at 4 °C. The supernatant was collected for further measurement. For binding capacity of nanoparticles with cytokines produced by damaged CMs and ECs, a Transwell model was built by seeding CMs onto the lower layer and ECs onto the upper layer. This Transwell system was treated with oxygen-glucose deprivation (OGD) for 12 h. Then NM@miR, RM@miR, MSNs@miR, and NM@miR plus inhibitor of certain cytokine receptor at different concentrations were added in the medium alone for 2 h. Then the medium of lower chamber was collected and centrifugated at 20,000 rpm for 20 min at 4 °C. The supernatant was collected for further measurement. For binding capacity of nanoparticles with cytokines *in vivo*, 6−8 weeks old C57BL/6 mice were subjected to mouse MI/R injury model. PBS, NM@miR, RM@miR, or MSNs@miR was systemically administrated 24 h after the injury. Mice were executed 48 h after injection. The blood was collected from the left ventricle and centrifuged at 3000 rpm for 10 min at 4 °C to collect serum. And the serum was centrifuged at 3000 rpm for 20 min at 4 °C. The supernatant was collected for further analysis. For quantification of the concentration of cytokines, the above-mentioned samples were measured using murine IL-1β, IL-6 and TNF-α ELISA Kit (Biolegend, San Diego, CA, USA).

2.12. Pharmacokinetics of NM@miR

8 weeks mice were tail vein injected with MSNs@miR or NM@miR, with miRNA was fluorescence conjugated. At different time points (0, 5, 15 and 30 min; 1, 3, 6, 18, 24, 48 and 72 h) the blood samples of each group were obtained through submandibular veins, and the fluorescence intensity was measured by microplate reader. To figure out the distribution of nanoparticles in major organs, mice were performed MI/R surgery and systematic administrated with MSNs@miR or NM@miR 24 h post-surgery. The mice were sacrificed and perfused with 4% PFA at 3 h, 1, 3, and 7 days after administration. All the major organs (liver, spleen, brain, kidney, and lung) were removed and immediately kept in 4% PFA. *In vivo* IVIS spectrum imaging system (PerkinElmer lnc, Germany) was used to obtain images of major organs presenting fluorescence distribution. The excitation and emission wavelengths were set at 552 nm and 570 nm. After that the above hearts were then performed paraffin embedding and sections (5 μm) Then the paraffin sections were subjected to dewaxing and antigen retrieval, followed by permeabilization, blocked, and incubated with anti-cTnT antibody (Proteintech, Rosemont, IL, USA) overnight. The slides were incubated with secondary antibody (Invitrogen, Carlsbad, CA, USA) and imaged with confocal microscope.

2.13. Measurement of long-term therapeutic benefit of NM@miR

To measure cardiac function, transthoracic echocardiography was conducted using Visual Sonics Vevo 2100 at 4 h and 4 weeks after

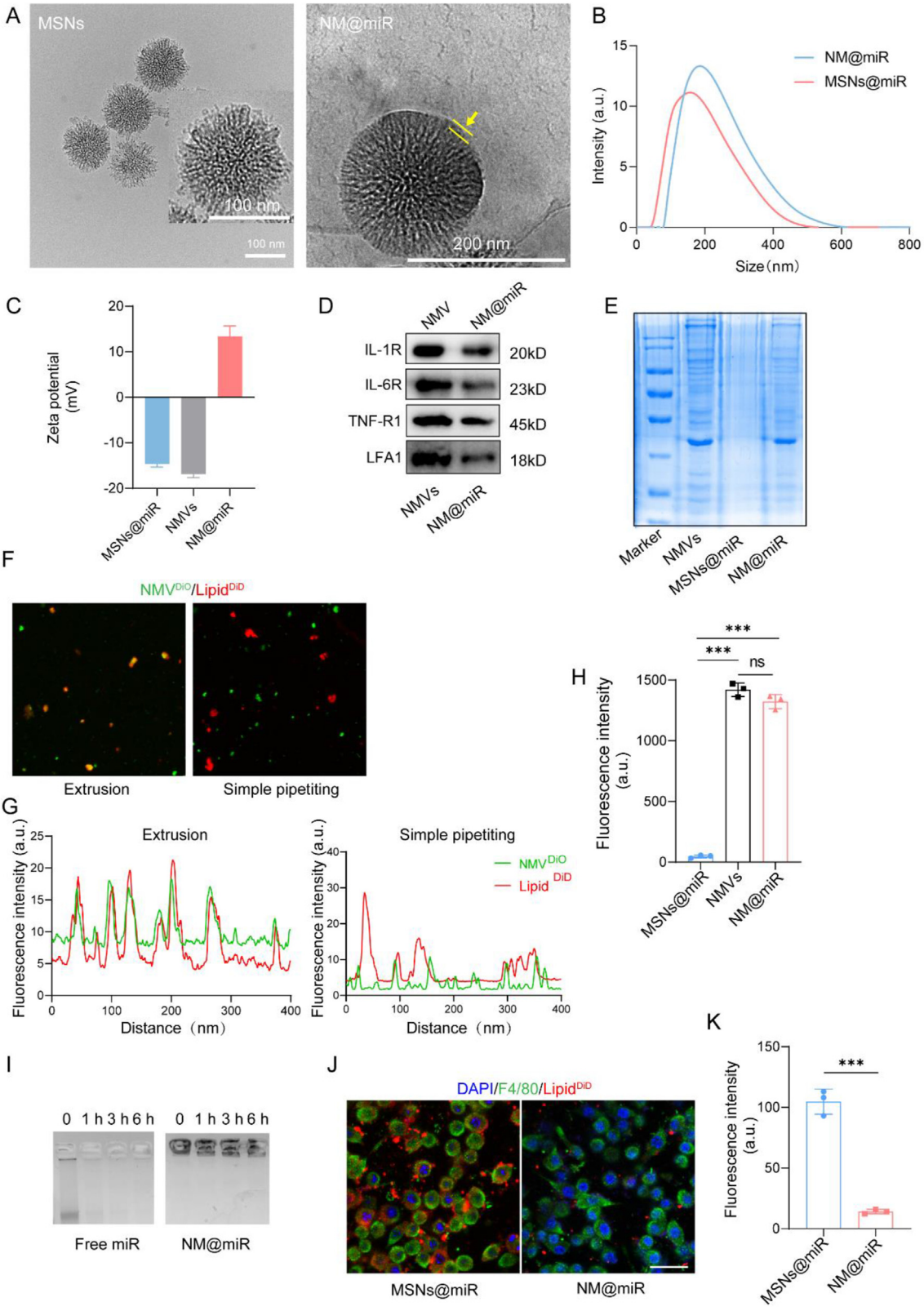

Figure 2 Fabrication and characterization of NM@miR. (A) Cryo-Transmission electron microscopy (Cryo-TEM) image of MSNs and NM@miR. (B) Diameters of MSNs@miR and NM@miR measured by dynamic light scattering (DLS) ($n = 3$). (C) Zeta potential of MSNs@miR and NM@miR ($n = 3$). (D) Western blots for neutrophil membrane protein (IL-1R1, IL-6R, TNF-R1 and LFA-1) in NMV or NM@miR. (E) Total protein profiles of NMVs and NM@miR stained with Coomassie Brilliant Blue. (F) Confocal images of NM@miR after extrusion (left) or simple pipetting (right) of NMV and MSNs@miR (Green, DiO-labeled NMVs; red, Cy3-labeled MSNs). (G) Qualitative analysis of the fluorescence colocalization between DiO-labeled NMVs and Cy3-labeled MSNs by image J software either after extrusion or after simple pipetting. (H) The

surgery. Two-dimensionally guided M-mode images of the short axis at the papillary muscle level were recorded. LVEF, LVFS, LVEDV, and LVESV were calculated in at least three consecutive cardiac cycles. After that, hearts were extracted, and subjected to paraffin embedding and section (7 μm). Masson's Trichrome staining was performed according to manufacturer's protocol (Abcam, Waltham, MA, USA) and analyzed for the infarct size and viable myocardium area using ImageJ-Fiji Software (National Institute of Health, USA).

2.14. Statistical analysis

Statistical analysis was performed using Graphpad Prism 8.0. The data was presented as mean ± SD, unless specific indication. Data following normal distribution was compared using the unpaired 2-tailed Student's *t*-test (2 groups). Comparisons between multiple groups were compared using One-way ANOVA. $P < 0.05$ was considered statistically significant.

3. Results and discussion

3.1. miR-10b expression decreases during heart development and affects CM proliferation in vitro

Though previous study has proved that miR-10b could promote proliferation of human embryonic stem cells-derived cardiomyocytes (hESC-CMs) by regulating the Hippo-YAP pathway, the effect of miR-10b on mouse CM has not yet been investigated. To confirm the regulatory effect of miR-10b on CM proliferation, we first evaluated the expression level of miR-10b in the mouse hearts at the time points of P1, P3, P5, P7, and P28 using quantitative real-time polymerase chain reaction (qRT-PCR) and found that miR-10b expression gradually decreased with the age increased (Supporting Information Fig. S1A), which is accompanied with the decreased proliferation capacity of neonatal mice hearts after birth[26]. Moreover, we also examined the expression changes of miR-10b after myocardial infarction (MI). As the results showed, miR-10b expression was downregulated in the border area of the injured heart (Fig. S1B). These results above may suggest that miR-10b might be a positive controller for CM proliferation. Next, neonatal mouse ventricular cardiomyocytes (neoCMs) were transfected with miR-10b mimic or negative control mimic using Lipofectamine RNAiMAX. After 48 h, immunofluorescence images revealed that miR-10b transfection led to an increase of EdU^+ (for DNA synthesis) and $pH3^+$ (for mitosis) neoCMs (Fig. S1C and D) and increased CMs numbers Fig. S1E, suggesting positive regulatory role of miR-10b on neoCMs proliferation. We previously reported that has-miR-10b-5p targets *LATS1* in hESC-CMs, the major component of Hippo pathway[8]. Herein, we identified that miR-10b is conservative between *Homo sapiens* and *Mus musculus* by bioinformatic prediction (Fig. S1F). The binding of miR-10b and 3′ UTR of *Lats1* in neoCMs was verified by dual-luciferase assay (Fig. S1G). Both mRNA and protein expression of *Lats1* in neoCMs were downregulated after transfection of miR-10b mimic (Fig. S1H and I). Furthermore, *Lats1* could promote phosphorylation of YAP protein in the cytoplasm, the important downstream component[27]. Here, treatment of miR-10b mimic could also decrease the phosphorylation of YAP protein in neoCMs (Fig. S1I and J). Taken together, the above data suggested that miR-10b could positively regulate neoCMs proliferation by targeting Hippo pathway.

3.2. Preparation and characteristic of NM@miR

To load with miR-10b, PEI-functionalized MSNs were first synthesized, which had positive charges. The Nitrogen adsorption-desorption isotherms and pore size distribution diagrams of MSN and PEI-MSN are shown in Supporting Information Fig. S2. Fluorescence labeled-miR was used to determine the loading efficiency of MSNs. It was demonstrated that miRNA could be encapsulated with high efficiency as the concentration of miRNA increased (Supporting Information Fig. S3). For the following study, 500 nmol/L miR-10b was chosen to constitute NM@miR. The membrane of TNF-α stimulated neutrophils were extracted following a previously reported method[28]. Next, the neutrophil-like hybrid membranes were prepared by the traditional hydration and extrusion method with artificial lipid and coated onto the MSNs@miR by co-extruded through porous membranes of decreasing sizes. To investigate the proper weight ratio between NMVs, artificial lipid and MSNs core, the hydrodynamic diameter and polydispersity index (PDI) were measured at different ratios. As the results showed, with the increasement ratio of NMVs, NM@miR presented enlarged size and reduced uniformity (Supporting Information Fig. S4A–C). We chose the NMVs-lipid-MSNs weight ratio 1:2:1 in the following study. Transmission electron microscopy (TEM) images (Fig. S4D) and Cryo-TEM images (Fig. 2A) confirmed the membrane layer onto the surface of MSNs. Consistent with this, dynamic light scattering measurements also revealed about 20 nm increase of diameters after membrane coating (Fig. 2B). The zeta potential of NM@miR exhibited a similar tendency with NMVs (Fig. 2C). These results above indicated the successful packaging of NM@miR. Western blot results showed that several main cytokine ligands (IL-1R1, IL-6R, and TNF-R1) and chemokine ligand (LFA-1) expressed onto the surface of NM@miR, similar to those which expressed on NMV (Fig. 2D), suggesting successful translocation of NMV onto the MSNs@miR, which was further proved by Coomassie Brilliant Blue staining (Fig. 2E). Furthermore, the colocalization of NMV fluorescence signal (DiO) and lipid fluorescence signal (DiD) through our extrusion method rather than simple pipetting also confirmed the successful fusion of NMV and MSNs@miR by confocal imaging (Fig. 2F and G). The colloidal stability of the MSNs@miR and NM@miR were also investigated and results revealed that both of them hold good colloidal stability in PBS with or without 10% FBS (Supporting Information Fig. S5A and B). More importantly, the prerequisite for maintaining inflammation-targeting properties is the right-side-out orientation of those membrane proteins. We then performed wheat germ agglutinin (WGA) staining to verify the sidedness of neutrophil membrane protein coating. NM@miR represented a similar fluorescence profile with natural NMV while bare MSNs@miR did

orientation of membrane protein in MSNs@miR, NMVs and NM@miR measured by Texas red conjugated WGA ($n = 3$). (I) Degradation of microRNA under the protection of biomimetic membrane or in the free form at different time points measured by agarose electrophoresis. (J) Representative confocal images of Raw 264.7 macrophages incubated with MSNs@miR or NM@miR for 24 h (Blue, nuclei; green, F4/80; red, Cy3-labeled MSNs). (K) Quantification of nanoparticles uptake by macrophages ($n = 3$). All data are shown as the mean ± SEM. ***$P < 0.001$ *vs*. indicated, ns, no significance. Scale bar = 50 μm.

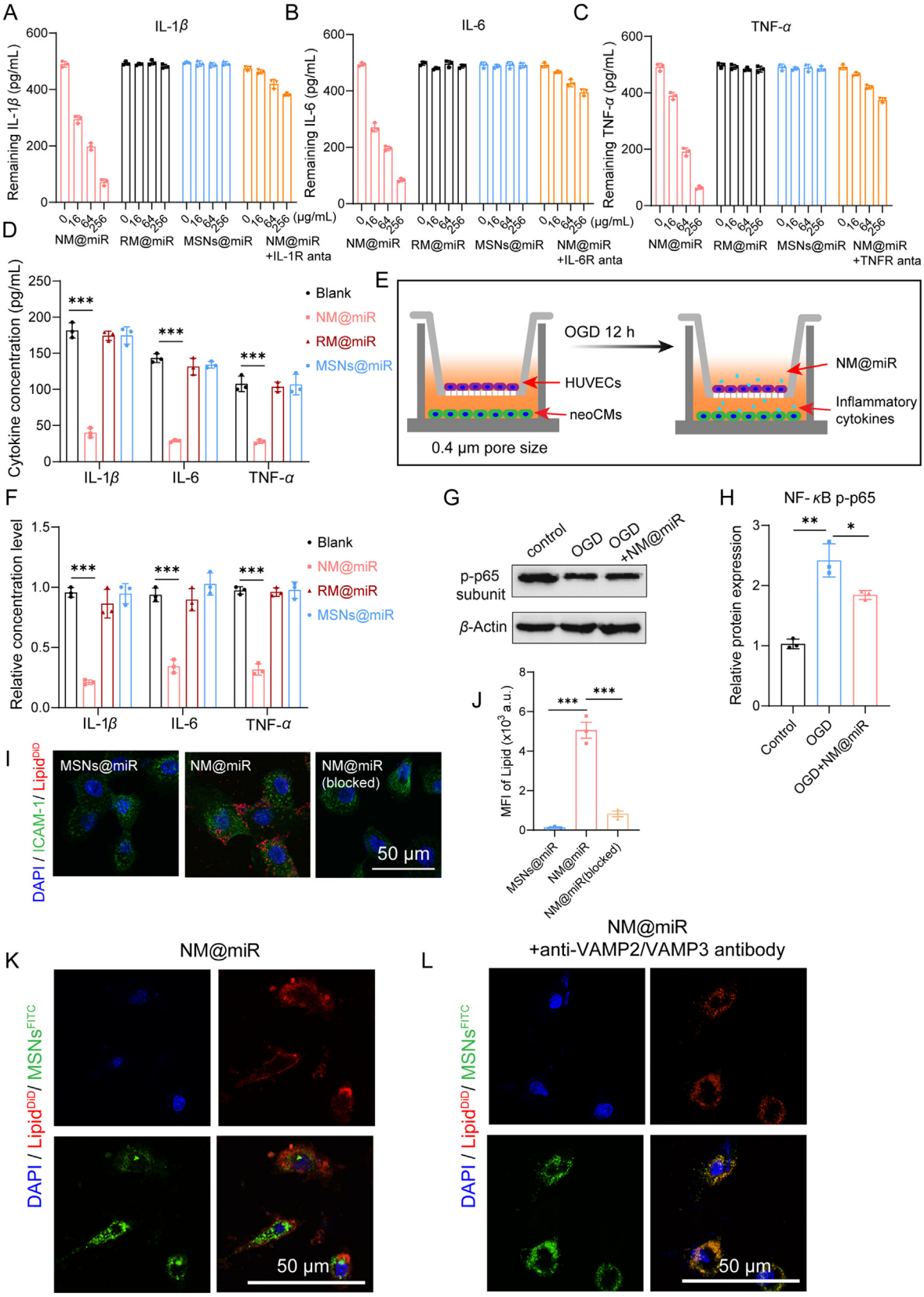

Figure 3 *In vitro* cytokine absorbing ability and inflammation homing ability of NM@miR. (A–C) binding capacity of NM@miR, RM@miR, bare MSNs@miR and NM@miR pretreated with IL-1R1, IL-6R, or TNF-R1 antagonist with IL-1β, IL-6, and TNF-α cytokine (500 pg/mL) ($n = 3$). (D) Concentration of proinflammatory cytokines (IL-1β, IL-6, and TNF-α) in the serum samples after mouse cardiac I/R injury incubated with NM@miR, RM@miR, or MSNs@miR ($n = 3$). (E) Schematic illustration of the *in vitro* model to evaluate the binding capability of

not (Fig. 2H), indicating the right-side-out neutrophil membrane protein orientation on the surface of NM@miR. MiRNAs are prone to be degraded by endogenous RNases, which hampers therapeutic application to a large extent when it comes to *in vivo* delivery[29]. Here, our combination of hybrid biomimetic membrane and miR-loaded MSNs could overcome this barrier and realized efficient delivery of miRNAs to the targeted sites. NM@miR or free miRNA was incubated with RNases for increasing time points and loaded onto the agarose gel. As the gel image showed, little degradation was observed under the protection of biomimetic membrane, indicating the ability of biomimetic membrane and dendritic MSNs to preserve the integrity of miRNA (Fig. 2I). We also found that the biomimetic membrane reduced the uptake of the nanoparticles by macrophages. After 24 h incubation with Raw 264.7 macrophages, fluorescence images demonstrated that there was much fewer uptake of NM@miR than MSNs@miR alone, probably owing to our neutrophil-mimicking strategy, which may imply possible well behavior of NM@miR in the blood circulation (Fig. 2J and K). Moreover, we constructed the fluorescence intensity quenching curve at different time points of the nanoparticles with different concentration of fluorescence (manipulated by adding different ratio of DiD-DSPE-PEG during synthesis). As indicated from the quenching curve (Fig. S5C), when the ratio of DiD-labeled lipid is more than 5%, the chance for concentration quenching would increase a lot. Therefore, we always chose less than 5% DiD-DSPE-PEG in the synthesis of fluorescence-labeled NM@miR.

3.3. *In vitro cytokine absorbing and inflammation homing ability of NM@miR*

Next, we sought to test the ability of NM@miR to absorb IL-1β, IL-6 and TNF-α, which play important roles in the inflammation process of cardiac ischemic injury. Red blood cell (RBC) membrane coated MSNs@miR (RM@miR) was used as control to highlight the cytokine absorbing ability mediated by neutrophil membrane receptors, as there are no such cytokine receptors on the RBC membrane. *In vitro* binding assays revealed that NM@miR could absorb those proinflammatory cytokines with the concentration increased, and no such results were observed when incubated with RM@miR and bare MSNs@miR (Fig. 3A–C). The concentration of cytokines was optimized by a series of preliminary experiments and the concentration of 500 pg/mL was used in the following study (Supporting Information Fig. S6A–S6C). These cytokine-inhibition effects were vanished when pre-incubated with inhibitor of certain cytokine receptor (IL-1R1, IL-6R, and TNF-R1) as control, which confirmed the specific cytokine-binding capacity mediated by cytokine receptor on the NM@miR. The ability of NM@miR to eliminate cytokines was further tested with mouse serum samples after MI/R surgery. Similar results were observed that proinflammatory cytokines levels in the serum decreased after incubation with NM@miR (Fig. 3D). To mimic *in vivo* immune microenvironment after cardiac ischemic injury, a Transwell model was constructed as shown in Fig. 3E. After oxygen-glucose deprivation (OGD) treatment for 12 h, concentration of IL-1β, IL-6 and TNF-α in the lower chamber medium elevated. However, concentration of cytokines decreased with NM@miR added to the medium (Fig. 3F). NM@miR treatment did not elevate the concentration of those inflammatory cytokines inside the cardiomyocytes as measured by enzyme linked immunosorbent assay (ELISA) of intracellular cytokines, which suggested that the adsorbed cytokines won't be internalized into the CMs (Fig. S6D). Moreover, transcription factor NF-κB plays a pivotal role in inflammation and shares a positive-feedback circuit with the synthesis of cytokines[30]. Therefore, as shown in the Western blot, protein expression level of NF-κB in neoCMs indeed lowered after treatment with NM@miR, which could avoid inflammatory response amplification by absorbing excessive proinflammatory cytokines (Fig. 3G and H). Redundant proinflammatory cytokines could also mediate the recruitment of leukocytes including neutrophils and Ly6C^{High} monocytes after cardiac ischemic injury which could release more inflammatory cytokines to amplify inflammation. The upper chamber of the constructed Transwell model was plated with neutrophils or LPS-stimulated Raw 264.7 macrophages rather than ECs to simulate the inflammation chemotaxis *in vitro* (Supporting Information Fig. S7A). As predicted, the number of migrated neutrophils increased a lot after OGD treatment of CMs in the lower chamber. However, pre-incubation with NM@miR inhibited this effect, which implied that NM@miR might reduce leukocytes recruitment by absorbing proinflammatory cytokines (Fig. S7B and C). After confirming the proinflammatory cytokines neutralization and ability of NM@miR, we began to explore its inflammation-homing ability, as there is a concentration gradient of cytokines between the infarcted myocardium and the normal region. The Transwell model with endothelial cells in the upper layer and smaller pore size (0.4 μm) was utilized and fluorescence labeled NM@miR was added to the upper chamber. As presented in the immunostaining results, NM@miR exhibited an inflammation-homing tendency and adhered to the ECs, probably mediated by the interaction between LFA-1 on the surface of NM@miR and ICAM-1 on the activated endothelium, which was further verified by blocking this interaction with anti-LFA-1 antibody (Fig. 3I and J). After successfully migrating the endothelial barrier, the fusion of hybrid membrane and the cardiomyocyte membrane, which attributed to the addition of cationic artificial lipid DOTAP, let the release of miRNA loaded MSNs into the cytosol, as shown in Fig. 3K, after incubating with NM@miR (DiD labeled lipid; Fluorescein isothiocyanate (FITC) labeled MSNs) for 6 h. Red DiD fluorescence signals of lipid mostly appeared on the surface of cardiomyocyte while green FITC signals of MSNs appeared in the cytoplasm. Soluble *N*- ethylmaleimide-sensitive factor attachment protein receptor (SNARE) proteins were previously reported to play a key role in the process of membrane fusion, such as vesicle-associated membrane protein 2 and 3 (VAMP2 and VAMP3)[31,32].

NM@miR using a transwell assay (0.4 μm pore size). (F) Concentration of proinflammatory cytokines (IL-1β, IL-6, and TNF-α) in the lower chamber of the transwell model under OGD treatment for 12 h ($n = 3$). (G) Western blotting analysis of NF-κB expression of neoCMs in the normal condition and OGD treatment with or without NM@miR preincubated. (H) Quantification of relative protein expression of NF-κB ($n = 3$). (I) Representative of ECs incubated with MSNs@miR, NM@miR or NM@miR pretreated with anti-LFA-1 antibody (Blue, nuclei; green, ICAM-1; red, DiD-labeled lipid). (J) Quantification of mean fluorescence intensity (MFI) of DiD lipid in different groups ($n = 3$). (K) Representative of CMs incubated with NM@miR after 6 h (Blue, nuclei; green, FITC-MSNs; red, DiD-labeled lipid). (L) Representative of CMs incubated with Anti-VAMP2 and VAMP3 antibody-pretreated NM@miR after 6 h (Blue, nuclei; green, FITC-MSNs; red, DiD-labeled lipid). All data are shown as the mean ± SEM. $^{*}P < 0.05$, $^{**}P < 0.01$, $^{***}P < 0.001$ *vs.* indicated; ns, no significance. Scale bar = 50 μm.

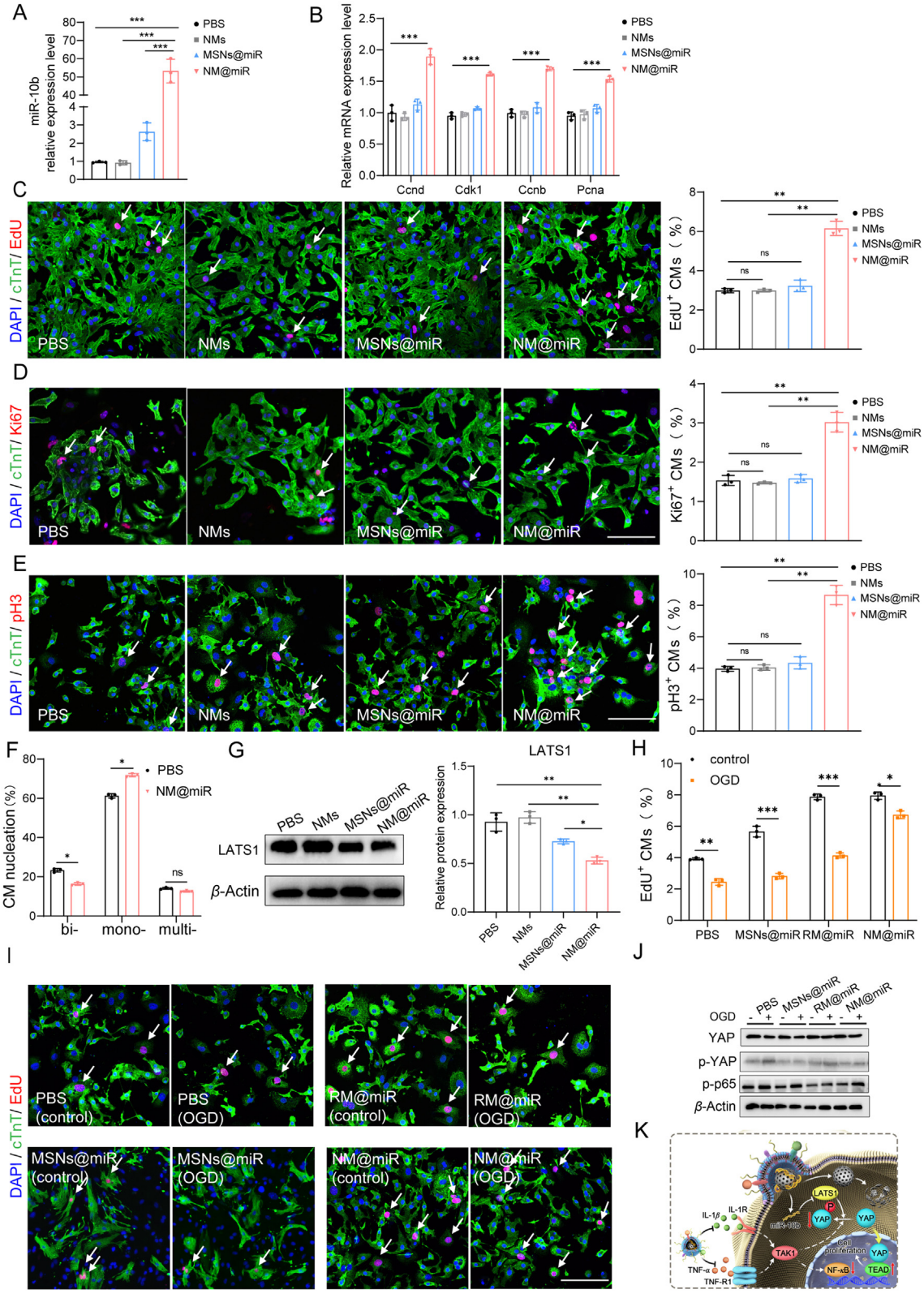

Figure 4 Roles of NM@miR on CMs proliferation under inflammation *in vitro* by regulating Hippo pathway. (A) Relative expression of miR-10b in neoCMs after 48 h treatment of PBS, NMs, MSNs@miR or NM@miR compared with internal control U6 ($n = 3$). (B) Relative mRNA expression of cell cycle-related genes (CCND, CDK1, CCNB, PCNA in neoCMs after 48 h treatment of PBS, NMs, MSNs@miR, NM@miR compared with internal control β-actin ($n = 3$). (C) Representative immunofluorescence images of neoCMs stained with cTnT (green) and EdU (red), and quantitative analysis of EdU$^+$ CMs ($n = 3$). (D) Representative immunofluorescence images of neoCMs stained with cTnT (green) and Ki67 (red), and quantitative analysis of Ki67$^+$ CMs ($n = 3$). (E) Representative immunofluorescence images of neoCMs stained with cTnT

To further prove the presence of membrane fusion, we pretreat NM@miR with VAMP2 and VAMP3 antibody and then incubated the nanoparticles with neoCMs. Immunofluorescent images suggested that the membrane fusion process may be impaired under the treatment of specific antibody as the red fluorescence signals of lipid, emerged on the cell surface, almost colocalized with green fluorescence signals of MSNs, which indicated different way of CMs to uptake NM@miR (Fig. 3L). Taken together, these data suggest that NM@miR holds the inflammation home ability and can migrate across the endothelium, followed by membrane fusion with cardiomyocytes and release of miRNA loaded MSNs into the cytosol.

3.4. *Roles of NM@miR on CMs proliferation under inflammation in vitro by regulating Hippo pathway*

Upon confirming the cytokine absorbing and inflammation targeting ability of NM@miR, the effect of therapeutic payload miR-10b was evaluated. We first measured the expression level of miR-10b after incubating neoCMs with NMs (neutrophil membrane coated MSNs without loading miR) MSNs@miR, or NM@miR for 48 h without OGD treatment. qRT-PCR results revealed that NM@miR treatment elevated the expression level of miR-10b in the CMs, indicating successful delivery of payload into the cells by our nanocarrier (Fig. 4A). Moreover, mRNA expression of cell-cycle related genes (*Ccnd, Cdk1, Ccnb, Pcna)* upregulated in the group of NM@miR, which represented high capacity of proliferation for neoCMs (Fig. 4B). This was further verified by co-immunostaining of EdU (for DNA synthesis), Ki67 (for cell cycle activity) and pH3 (for mitosis) with cTnT, the specific marker for CMs. We found that the percentage of double positive CMs increased a lot after NM@miR treatment (Fig. 4C−E). Importantly, the percentage of binucleated CMs increased while there was a percentage decrease of multinucleated CMs (Fig. 4F), demonstrating that percentage of CMs with proliferative capacity increased, which was consistent with our previous research[8]. Next, we examined the effects of nanoparticles on Hippo pathway in neoCMs. The mRNA expression of *Lats1* was downregulated as confirmed by qRT-PCR (Supporting Information Fig. S8A). Western blotting results further revealed that NM@miR lower the expression of LATS1 at the protein level (Fig. 4G), while NMs and MSNs@miR showed no effect on the expression of LATS1, suggesting that our biomimetic nanocarrier could successfully deliver miR-10 into the CMs and promote proliferation through Hippo pathway by targeting *Lats1* without inflammatory condition. We next investigated the impact of cytokine absorbing on the NM@miR' s proliferative capacity under inflammation to measure the advantage of our combination strategy. In the Transwell model with endothelial cells in the upper layer, neoCMs were treated OGD and preincubated with NM@miR, RM@miR or MSNs@miR. It has been reported that proinflammatory cytokines (IL-1β or TNF-α) could stimulate YAP/TAZ degradation and activate Hippo pathway[3,10]. Here, with elevated level of proinflammatory cytokines by OGD treatment, immunostaining results of EdU^+ or $pH3^+$ CMs indicated that OGD treatment led to impaired proliferative effect of miR-10b, further resulting in proliferation of CMs without any intervention, and only under neutralization effect mediated by biomimetic neutrophil membrane rather than erythrocyte membrane, the proliferative capacity of miR-10b could be partly recovered (Fig. 4H and I). We further confirmed decrease expression of total YAP protein and increased phosphorylation in neoCMs under inflammation (Fig. 4J and Fig. S8B and C), as elevated inflammatory cytokines trigger the degradation of YAP and activation of Hippo pathway. This change was partly reversed under the treatment of NM@miR (Fig. 4J). Moreover, we also found that under NM@miR, recovery of Yap protein could attenuate NF-κB signaling, as shown in western blotting data of phosphorylation of p65 subunit (Fig. 4J and Fig. S8D). These data together suggested positive feedback might exist after our NM@miR treatment to restrain excessive inflammation and promote neoCMs proliferation (Fig. 4K), which is likely to present well therapeutic effect *in vivo*.

3.5. *Apoptosis of neoCMs could be reduced by NM@miR*

MiR-10b was reported to protect hESCs-CMs from apoptosis[8]. Here, TUNEL staining suggested that NM@miR could reduce apoptosis of CMs more effectively than RM@miR (Supporting Information Fig. S9A and B) mainly because of combinational function between the anti-apoptosis effect of miR-10b and improved microenvironment resulted from absorbing of proinflammatory cytokines. Furthermore, protein expression of apoptosis-related genes (BCL-2, BAX, CASPASE 3) validated above-mentioned results (Fig. S9C−F). These results demonstrated that NM@miR could protect neoCMs from apoptosis.

3.6. *In vivo targeting profile of NM@miR*

Next, we evaluated the *in vivo* behavior of NM@miR by using fluorescence-labeled nanoparticles. Firstly, blood circulation profile of NM@miR was investigated. As shown in the Supporting Information Fig. S10A, NM@miR exhibited longer circulation time within 72 h than bare MSNs@miR, possibly because this hybrid biomimetic membrane coating could reduce elimination by the monocytes/macrophage system. After that, the biodistribution of NM@miR in the major organs (heart, liver, spleen, lung, kidney, and brain) was quantified by using *Ex Vivo* Imaging System in a mouse cardiac I/R injury model. The injury model was constructed by a traditional method with minimal adjustment[33]. Like most of other nanoparticles, NM@miR and RM@miR were found

(green) and pH3 (red), and quantitative analysis of $pH3^+$ CMs ($n = 3$). (F) Quantification of nucleus after treatment of PBS or NM@miR. 500 $cTnT^+$ cells were analyzed per replicate ($n = 3$). (G) Western blotting images and Quantification of relative LATS1 expression of neoCMs under treatment of PBS, NMs, MSNs@miR, or NM@miR. (H) Quantification of EdU^+ CMs with or without OGD treatment under incubation with PBS, MSNs@miR, RM@miR, or NM@miR ($n = 3$). (I) Representative confocal images of neoCMs with or without OGD treatment, and incubation with PBS, MSNs@miR, RM@miR or NM@miR (Blue, nuclei; green, cTnT; red, EdU). (J) Western blotting images of relative YAP, p-YAP, and NF-κB p-p65 subunit expression of neoCMs under incubation of PBS, MSNs@miR, RM@miR, or NM@miR, with or without OGD treatment, compared with β-actin as internal control ($n = 3$). (K) Schematic Illustration of NM@miR to elevate inflammation and promote proliferation through Hippo pathway and NF-κB pathway. All data are shown as the mean ± SEM. $^*P < 0.05$, $^{**}P < 0.01$, $^{***}P < 0.001$ *vs.* indicated; ns, no significance. Scale bar = 50 μm.

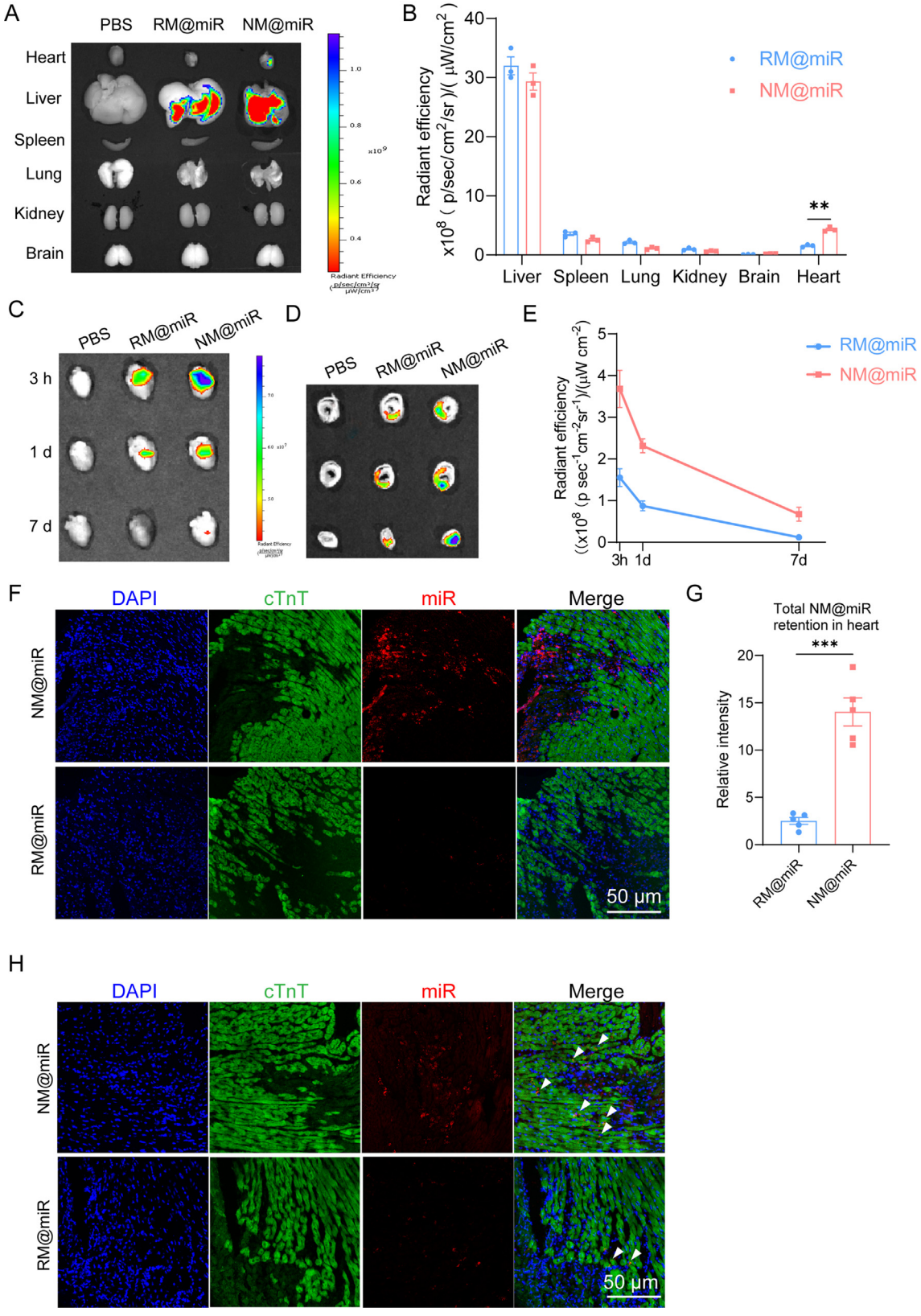

Figure 5 *In vivo* targeting profile of NM@miR. (A) *Ex vivo* fluorescent imaging of major organs 3 h after intravenous injection with PBS, fluorescence labeled RM@miR or NM@miR. (B) Quantification of nanoparticles accumulation in major organs 3 h after intravenous administration ($n = 3$). (C) Representative *ex vivo* fluorescent images of the hearts at different time points after intravenous injection with PBS, RM@miR, NM@miR. (D) Represent *ex vivo* fluorescent images of thick heart sections 3 h after different treatments. (E) Quantification of nanoparticles accumulation in the injured hearts at different time points (3 h, 1 d and 7 d) after systemic administration with RM@miR or

to preferentially accumulate in the liver with the increase of time (Fig. 5A and B). However, hybrid neutrophil-like membrane coating could reduce accumulation in the liver and increase the possibility of targeting to the injured heart. As shown in Fig. 5C and D, NM@miR treatment showed more nanoparticles and longer time retention in the injured heart. Specifically, cross sections of the hearts in the NM@miR group presented the same tendency of infarcted area targeting (Fig. 5E). Following that, we performed immunofluorescent assay on frozen sections of the hearts. Co-staining images of cTnT (for CMs) indicated that fluorescence-labeled NM@miR first mainly distributed in the border region between the infarct and intact myocardium 3 h after intravenous injection, compared with little distribution of RM@miR (Fig. 5F and G). We observed further uptake of NM@miR by local CMs 12 h after injection (Fig. 5H). Flow cytometry analysis of percentage of $cTnT^+$ DiD^+ (Fig. S10B and C) cells revealed that after being recruited into the infarcted area, NM@miR could be uptake by endogenous CMs to exert the following effect. These data demonstrated that NM@miR could be recruited to the inflammation sites, transmigrated over the activated endothelium, and uptake by CMs, on account of inflammation-targeting property endowed by "parental" neutrophils.

3.7. *Reconstruction of post-injury immune microenvironment and enhancement of CMs proliferation by NM@miR in vivo*

After confirming the *in vivo* targeting profile, we evaluated the *in vivo* therapeutic effect of NM@miR using the same mouse cardiac I/R injury model. NM@miR was administered intravenously one day after injury (D1). We found out both the serum level and the myocardium concentration of IL-1β, IL-6, and TNF-α were indeed elevated within 3 days after cardiac ischemic injury (Supporting Information Fig. S11A and B), indicating the rationality of our study. RM@miR and NMs was selected as controls to highlight the advantage of cytokine neutralization mediated by neutrophil membrane fusion and the proliferative capacity of miR-10b. Other controls were omitted due to their poor potency for therapy *in vitro* studies. Short-term (within a week) and long-term (4 weeks) benefits were both evaluated to assess the potential therapeutic effect of NM@miR. For the short-term benefits, the ability of proinflammatory cytokine absorbing was first evaluated. 48 h after the administration, the level of three major cytokines (IL-1β, IL-6, and TNF-α) in the serum and in the tissue, both decreased in the NM@miR group, which was not observed under treatment of RM@miR (Fig. 6A and B). In accordance with decrease of those proinflammatory cytokines, the protein level of transcription factor NF-κB downregulated, which suggested successful blockade of intense inflammation cascade (Fig. 6C and D). Infiltration of $CD45^+$ leukocytes was alleviated as shown in the flow cytometry data (Fig. 6E). These results mentioned above proved that NM@miR surely could restrain excessive inflammation and restore local immune microenvironment, which was based on absorbing proinflammatory cytokines. Next, anti-apoptosis effect of NM@miR was investigated. Five days after injury, NM@miR treatment led to a reduction of apoptotic cells in the border zone as revealed by immunofluorescence TUNEL staining (Fig. 6F). NM@miR provided much more protection effect against apoptosis than RM@miR and NMs, probably because of combination of cytokine absorption and miR-10b's itself anti-apoptosis effect. Upon confirming the immunity modulation ability of NM@miR mediated by neutrophil membrane, the proliferative capacity mediated by the therapeutic payload miR-10b was further evaluated. The expression level of markers for CMs proliferation including EdU, Ki67 (co-stained with cTnT, marker for CMs) was measured in groups receiving different treatment. Immunofluorescence staining images showed that NM@miR led to a much higher (around 3-fold) level of CMs proliferation than PBS and NMs treatment, and fairly higher (around 2-fold) level than RM@miR group (Fig. 6G and H), which demonstrated the combinational effect between cytokines neutralization and miRNAs' proliferative function to enhance therapeutic benefits of our nanoparticles.

3.8. *Improvement of cardiac function and alleviation of fibrosis after NM@miR treatment*

Long term benefits of NM@miR therapy were figured out 4 weeks after injury. Noninvasive transthoracic echocardiography was used to measure the cardiac function of mice receiving different treatments, and the cardiac function at 4 h post injury was measured as baselines. Echocardiography results revealed improved left ventricular (LV) ejection fractions (LVEF) and LV fractional shortening (LVFS) as well as decreased LV end-diastolic volume (LVEDV) and LV end-systolic volume (LVESV) in the NM@miR group, reflecting recovery of cardiac function (Fig. 7A−D). What's more, Masson's trichrome-staining of the hearts showed that more viable myocardium and fewer fibrosis area were observed after NM@miR treatment, in keeping with ameliorated cardiac function (Fig. 7E−G). These data indicated that combination therapy of immunity modulation and CMs proliferation in the short term could result of decent therapeutic effect in the long term.

3.9. *Biosafety evaluation of NM@miR therapy*

The *in vitro* and *in vivo* biosafety issues of NM@miR were investigated. NeoCMs and ECs were incubated with NM@miR for 24 h and cell viability/toxicity were measured under Confocal microscope. As showed in Supporting Information Fig. S12A and 12B, viability of cells was not affected, and no significant toxic reaction was observed after NM@miR treatment. NM@miR was also administered to healthy C57 mice to evaluate *in vivo* biocompatibility. The expression level of inflammatory cytokines (IL-1β, IL-6, and TNF-α) did not elevated in the serum of mice injected of NM@miR, compared to mice injected of PBS, suggesting no obvious inflammation response caused by this biomimetic nanosponge (Fig. S12C−12E). Hematoxylin-eosin (HE) staining of the major organs also revealed negligible systemic toxicity, suggesting good biosafety of NM@miR (Fig. S12F).

NM@miR ($n = 3$). (F) Confocal images of NM@miR or RM@miR in the infarcted hearts 3 h after injection (Blue, nuclei; green, cTnT; red, Did-labeled nanoparticles). (G) Quantification of nanoparticles retention in the border area of the infarcted myocardium 3 h after injection ($n = 3$). (H) Confocal images of NM@miR or RM@miR in the infarcted hearts 12 h after injection (blue, nuclei; green, cTnT; red, DiD-labeled nanoparticles). All data are shown as the mean ± SEM. $^*P < 0.05$, $^{**}P < 0.01$, $^{***}P < 0.001$ *vs.* indicated. Scale bar = 50 μm.

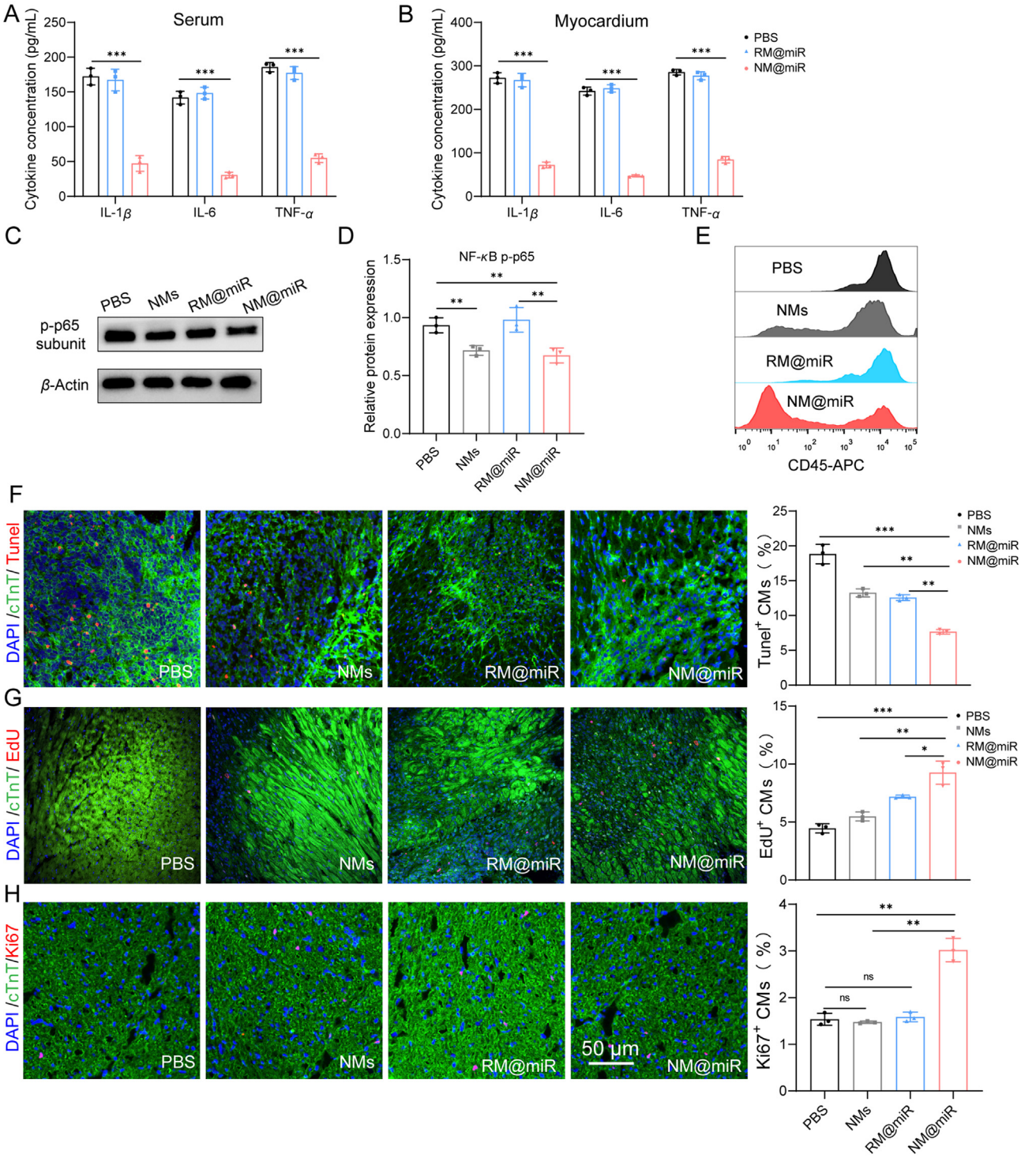

Figure 6 Reconstruction of post-injury immune microenvironment and enhancement of CMs proliferation by NM@miR *in vivo* (A, B) Concentration of proinflammatory cytokines (IL-1β, IL-6, and TNF-α) in the serum and injured myocardium of mice injected with PBS, RM@miR, NM@miR after cardiac I/R injury ($n = 3$). (C) Western blotting assay of phosphorylation NF-κB p65 subunit expression of injured myocardium. (D) Quantification of relative protein expression of phosphorylation NF-κB p65 compared with β-actin as internal control ($n = 3$). (E) Flow cytometry analysis of $CD45^+$ leukocytes infiltration in the myocardium after systemic administration of PBS, NMs, RM@miR, or NM@miR (stained with APC-anti-CD45 antibody). (F) Representative images and quantitative measurement of CMs apoptosis in the injured myocardium as stained with TUNEL staining ($n = 3$). (G, H) Representative images and quantitative measurement of CMs proliferation in the injured myocardium as stained by EdU and Ki67 staining ($n = 3$). All data are shown as the mean ± SEM. $^*P < 0.05$, $^{**}P < 0.01$, $^{***}P < 0.001$ *vs*. indicated; ns, no significance. Scale bar = 50 μm.

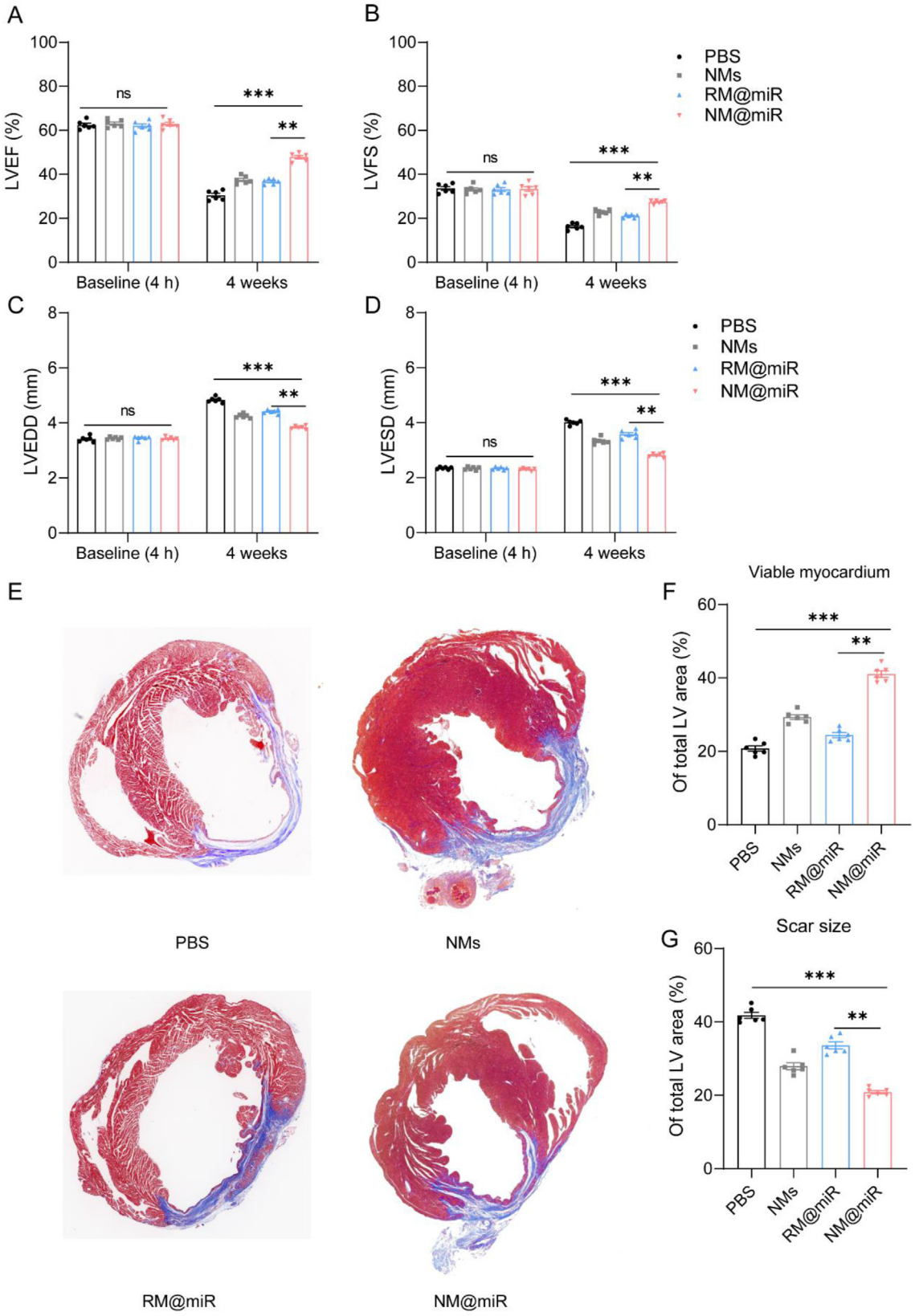

Figure 7 Improvement of cardiac function and alleviation of fibrosis after NM@miR treatment. (A−D) LVEF, LVFS, LVEDD, and LVESD measured by echocardiography at baseline (4 h) and 4 weeks after I/R injury, treated with PBS, NMs, RM@miR, or NM@miR ($n = 6$). (E) Masson's Trichrome staining of the mice hearts 4 weeks after I/R injury. (F−G) Quantitative assessment of the percentages of viable myocardium or scar tissues in the Masson's trichrome staining images ($n = 6$). All data are shown as the mean ± SEM. $^{**}P < 0.01$, $^{***}P < 0.001$ *vs.* indicated; ns, no significance.

3.10. Discussion

Here, we developed neutrophil membrane-coated nanosponges that were able to neutralize excessive proinflammatory cytokines and deliver regenerative molecules to manipulate Hippo pathway at the same time. In the research, we chose MSNs, which are biodegradable and hold large volume to deliver nuclei acids, as carriers for miR-10b, a therapeutic microRNA reported to promote CMs proliferation. The degradation of MSNs undergoes a two-stage process that can last around 72 h, with rapid degradation for the outside shells in the first stage and a slow degradation process in the second stage[25]. What's more, MSNs are cleared mainly by liver and kidney after injection[34–36]. However, redundant proinflammatory cytokines in the acute stage of cardiac ischemic injury may impair CMs proliferation mediated by miR-10b, which is led by increase degradation of Yap protein[10,11]. Traditional methods targeting a single specific cytokine or chemokine may have a limited effect as several cytokines and chemokines may share compensation mechanisms after cardiac injury. Thus, we introduced neutrophil-mimicking strategy to absorb multiple proinflammatory cytokines by taking advantage of receptor proteins expressed on the neutrophil membrane. Our work also has some limitations. Although excessive proinflammatory cytokines constitute the microenvironment after cardiac ischemic injury and may cause more severe cascade harm to the surrounding tissue, too much neutralization of cytokines may bring about unwanted outcomes. Therefore, optimized density of neutrophil membrane protein on the biomimetic membrane should be determined to get the best therapeutic effect without leading to secondary harm. What's more, the underlying mechanisms need to be further explored as neutrophils membrane may serve as sources of pro-resolving lipid mediators, which may represent an alternative possible mechanism by which neutrophil membrane coated silica nanoparticles suppress inflammation. Moreover, to prove our concept of combinational therapy, human samples and large animal models are supposed to be included in the study to broad the translational potential of our work.

4. Conclusions

In summary, we use a nanoparticle-based method to reconstruct the immune microenvironment after cardiac I/R injury and to promote endogenous CMs proliferation. This neutrophil-mimic NM@miR can home to the injured myocardium, deliver miRNAs of proliferative capacity, neutralize excessive inflammatory cytokines, to promote heart regeneration by regulating Hippo-YAP pathway, thus mitigate fibrosis, and improve cardiac function. This work offers a biomimetic nanosystem to modulate local immunity, targeted delivery of therapeutic microRNA, and improved combined therapeutic efficacy. Our nanosponges show promising in overcoming challenges in current cardiac regeneration therapy and hold bright field for future clinical translation.

Acknowledgments

This work was financially supported by State Key Clinical Specialty Construction Project (YW2021-002, China), and the National Natural Science Foundation of China (Nos. 82070281, 81870269, and 81600199).

Author contributions

Qiaozi Wang and Jinfeng Gao performed most of the experiments and did the data analysis. Yanan Song wrote the original manuscript. Qiyu Li and Jing Chen provided help for *in vitro* experiment for cells. Yifang Xie and Zhengmin Wang finished modification for figures. Ning Zhang and Haipeng Tan provided some materials support. Juying Qian and Hongbo Yang provided suggestions on animal model constructions. Zhiqing Pang had supervision of all study. Zheyong Huang revised the manuscript. Junbo Ge conceived the project. All authors read and approved the final manuscript.

Conflicts of interest

The authors declare no conflicts of interest.

Appendix A. Supporting information

Supporting data to this article can be found online at https://doi.org/10.1016/j.apsb.2023.08.021.

References

1. Laflamme MA, Murry CE. Heart regeneration. *Nature* 2011;**473**:326–35.
2. Finan A, Richard S. Stimulating endogenous cardiac repair. *Front Cell Dev Biol* 2015;**3**:57.
3. Wang J, Liu SJ, Heallen T, Martin JF. The Hippo pathway in the heart: pivotal roles in development, disease, and regeneration. *Nat Rev Cardiol* 2018;**15**:672–84.
4. Lin ZQ, von Gise A, Zhou PZ, Gu F, Ma Q, Jiang JM, et al. Cardiac-specific YAP activation improves cardiac function and survival in an experimental murine MI model. *Circ Res* 2014;**115**:354–63.
5. Chen JM, Ma Q, King JS, Sun Y, Xu B, Zhang XY, et al. aYAP modRNA reduces cardiac inflammation and hypertrophy in a murine ischemia-reperfusion model. *Life Sci Alliance* 2020;**3**.
6. Yin VP, Lepilina A, Smith A, Poss KD. Regulation of zebrafish heart regeneration by miR-133. *Dev Biol* 2012;**365**:319–27.
7. Tian Y, Liu Y, Wang T, Zhou N, Kong J, Chen L, et al. A microRNA-Hippo pathway that promotes cardiomyocyte proliferation and cardiac regeneration in mice. *Sci Transl Med* 2015;**7**:279ra38.
8. Xie YF, Wang QZ, Gao N, Wu FJ, Lan F, Zhang F, et al. MircroRNA-10b promotes human embryonic stem cell-derived cardiomyocyte proliferation *via* novel target gene *LAST1*. *Mol Ther Nucleic Acids* 2020;**19**:437–45.
9. Eulalio A, Mano M, Dal Ferro M, Zentilin L, Sinagra G, Zacchigna S, et al. Functional screening identifies miRNAs inducing cardiac regeneration. *Nature* 2012;**492**:376–81.
10. Gao YN, Sun Y, Ercan-Sencicek AG, King JS, Akerberg BN, Ma Q, et al. YAP/TEAD1 complex is a default repressor of cardiac toll-like receptor genes. *Int J Mol Sci* 2021:22.
11. Deng YJ, Lu JQ, Li WL, Wu AL, Zhang X, Tong WX, et al. Reciprocal inhibition of YAP/TAZ and NF-κB regulates osteoarthritic cartilage degradation. *Nat Commun* 2018;**9**:4564.
12. Ridker PM, Everett BM, Thuren T, MacFadyen JG, Chang WH, Ballantyne C, et al. Antiinflammatory therapy with canakinumab for atherosclerotic disease. *N Engl J Med* 2017;**377**:1119–31.
13. Li ZH, Hu SQ, Huang K, Su T, Cores J, Cheng K. Targeted anti-IL-1β platelet microparticles for cardiac detoxing and repair. *Sci Adv* 2020;**6**.
14. Zhang QZ, Dehaini D, Zhang Y, Zhou J, Chen XY, Zhang LF, et al. Neutrophil membrane-coated nanoparticles inhibit synovial inflammation and alleviate joint damage in inflammatory arthritis. *Nat Nanotechnol* 2018;**13**:1182–90.
15. Hou MY, Wei YS, Zhao ZY, Han WQ, Zhou RX, Zhou Y, et al. Immuno-engineered nanodecoys for the multi-target anti-inflammatory treatment of autoimmune diseases. *Adv Mater* 2022;**34**:e2108817.
16. Zhou Y, Deng YK, Liu ZM, Yin MY, Hou MY, Zhao ZY, et al. Cytokine-scavenging nanodecoys reconstruct osteoclast/osteoblast

balance toward the treatment of postmenopausal osteoporosis. *Sci Adv* 2022;**7**:eabl6432.
17. Chen J, Song YN, Wang QZ, Li QY, Tan HP, Gao JF, et al. Targeted neutrophil-mimetic liposomes promote cardiac repair by adsorbing proinflammatory cytokines and regulating the immune microenvironment. *J Nanobiotechnol* 2022;**20**:218.
18. Farid M, Faber T, Dietrich D, Lamprecht A. Cell membrane fusing liposomes for cytoplasmic delivery in brain endothelial cells. *Colloids Surf, B* 2020;**194**:111193.
19. Cavalcanti RRM, Lira RB, Riske KA. Membrane fusion biophysical analysis of fusogenic liposomes. *Langmuir* 2022;**38**:10430−41.
20. Tan HP, Song YN, Chen J, Zhang N, Wang QZ, Li QY, et al. Platelet-like fusogenic liposome-mediated targeting delivery of miR-21 improves myocardial remodeling by reprogramming macrophages post myocardial ischemia-reperfusion injury. *Adv Sci* 2021:e2100787.
21. Kim B, Pang HB, Kang J, Park JH, Ruoslahti E, Sailor MJ. Immunogene therapy with fusogenic nanoparticles modulates macrophage response to Staphylococcus aureus. *Nat Commun* 2018;**9**:1969.
22. Slowing II , Vivero-Escoto JL, Wu CW, Lin VS. Mesoporous silica nanoparticles as controlled release drug delivery and gene transfection carriers. *Adv Drug Deliv Rev* 2008;**60**:1278−88.
23. Huang R, Shen YW, Guan YY, Jiang YX, Wu Y, Rahman K, et al. Mesoporous silica nanoparticles: facile surface functionalization and versatile biomedical applications in oncology. *Acta Biomater* 2020;**116**:1−15.
24. Kankala RK, Han YH, Na J, Lee CH, Sun ZQ, Wang SB, et al. Nanoarchitectured structure and surface biofunctionality of mesoporous silica nanoparticles. *Adv Mater* 2020;**32**:e1907035.
25. Shen DK, Yang JP, Li XM, Zhou L, Zhang RY, Li W, et al. Biphase stratification approach to three-dimensional dendritic biodegradable mesoporous silica nanospheres. *Nano Lett* 2014;**14**:923−32.
26. Porrello ER, Mahmoud AI, Simpson E, Hill JA, Richardson JA, Olson EN, et al. Transient regenerative potential of the neonatal mouse heart. *Science* 2011;**331**:1078−80.
27. Meng ZP, Moroishi T, Guan KL. Mechanisms of Hippo pathway regulation. *Genes Dev* 2016;**30**:1−17.
28. Fang RH, Hu CM, Luk BT, Gao W, Copp JA, Tai Y, et al. Cancer cell membrane-coated nanoparticles for anticancer vaccination and drug delivery. *Nano Lett* 2014;**14**:2181−8.
29. Ben-Shushan D, Markovsky E, Gibori H, Tiram G, Scomparin A, Satchi-Fainaro R. Overcoming obstacles in microRNA delivery towards improved cancer therapy. *Drug Deliv and Transl Res* 2014;**4**:38−49.
30. Liu T, Zhang LY, Joo D, Sun SC. NF-κB signaling in inflammation. *Signal Transduct Targeted Ther* 2017;**2**:17023.
31. Fix M, Melia TJ, Jaiswal JK, Rappoport JZ, You DQ, Söllner TH, et al. Imaging single membrane fusion events mediated by SNARE proteins. *Proc Natl Acad Sci U S A* 2004;**101**:7311−6.
32. Meyenberg K, Lygina AS, van den Bogaart G, Jahn R, Diederichsen U. SNARE derived peptide mimic inducing membrane fusion. *Chem* 2011;**47**.
33. Michael LH, Entman ML, Hartley CJ, Youker KA, Zhu J, Hall SR, et al. Myocardial ischemia and reperfusion: a murine model. *Am J Physiol* 1995;**269**:H2147−54.
34. Li LL, Liu TL, Fu CH, Tan LF, Meng XW, Liu HY. Biodistribution, excretion, and toxicity of mesoporous silica nanoparticles after oral administration depend on their shape. *Nanomedicine* 2015;**11**:1915−24.
35. He QJ, Zhang ZW, Gao F, Li YP, Shi JL. *In vivo* biodistribution and urinary excretion of mesoporous silica nanoparticles: effects of particle size and PEGylation. *Small* 2011;**7**:271−80.
36. Fu CH, Liu TL, Li LL, Liu HY, Chen D, Tang FQ. The absorption, distribution, excretion and toxicity of mesoporous silica nanoparticles in mice following different exposure routes. *Biomaterials* 2013;**34**:2565−75.